Roughness-induced transition in high speed flows

Prahladh S Iyer[*] , Suman Muppidi[†] and Krishnan Mahesh[‡]

University of Minnesota, Minneapolis, Minnesota, 55455, USA

Roughness elements in a laminar boundary layer can cause the flow to transition. The effects of discrete and distributed roughness are explored using direct numerical simulation on unstructured grids. Velocity profiles for Mach 8.12 flow past a cylindrical roughness element are compared to experiment.[1] Flow features produced by an isolated hemispherical bump are studied for three Mach numbers [3.37, 5.26, 8.23] whose simulation parameters are chosen to match the experiments performed by Danehy et al.[2] at NASA Langley. The vortices formed upstream of the roughness due to boundary layer separation wrap around the hemisphere generating coherent streamwise vortices. A significant increase in wall skin friction coefficient along with the presence of unsteady structures far downstream of the bump for the lower Mach number cases indicated the transitional/turbulent nature of the flow while M_∞=8.23 remained laminar. These observations are consistent with those in experiment. The effect of a sinusoidally varying distributed roughness was also investigated at M_∞=2.9. The flow transitioned to a fully developed turbulent boundary layer that shows good quantitative agreement with experimental data. The cumulative effect of multiple roughness elements is to decelerate the near wall fluid, and setup inflexional velocity profiles. For both types of roughness it was seen that: (1) coherent streamwise vortices were produced which broke down far downstream, (2) prominent hairpin shaped structures were observed as the flow transitioned and (3) wall normal and spanwise inflexion points in streamwise velocity are observed.

Nomenclature

ρ	Density	u	Velocity
p	Pressure	T	Temperature
E_T	Total Energy	σ_{ij}	Viscous shear stress
Q_i	Heat flux	M_∞	Free stream Mach number
Re	Free stream unit Reynolds number	Re_k	$\rho_\infty k u_\infty/\mu_\infty$
u_c	Van Driest transformed velocity	C_f	Skin friction coefficient
Subscript			
CV	control volume	k	roughness height
d	diameter	∞	free-stream

I.   Introduction

Transition causes undesirable increase in drag and heating rates. Both discrete and distributed roughness can cause an initially laminar flow to transition. Discrete roughness appears in the form of steps, joints, rivets and local machining flaws, and distributed roughness appears in the form of screw threads, patterns left on a metal surface by machining and finishing processes and ablation effects on the thermal protection system.[3] While empirical models like Re_θ/M^4 and Re_{kk}[5] are available for predicting transition, more accurate physics based models need to be developed. High-fidelity direct numerical simulations(DNS) can provide a comprehensive understanding of the various phenomena associated with transition.

---

[*]Graduate student, Dept. of Aerospace Engineering and Mechanics, University of Minnesota, MN 55455, Student member.
[†]Research Associate, Dept. of Aerospace Engineering and Mechanics, University of Minnesota, MN 55455, Member.
[‡]Professor, Dept. of Aerospace Engineering and Mechanics, University of Minnesota, MN 55455, Associate Fellow.

While incompressible transition is sensitive to Reynolds number and the shape and height of the roughness element, transition at supersonic speeds is also sensitive to the Mach number, freestream temperature and the thermal boundary condition at the wall. Also, the influence of shock waves produced by the roughness on transition location is still unclear. The effect of an isolated hemisphere on an incompressible laminar boundary layer was studied by Tani,[6] Dryden,[7] Klebanoff[8] and Acarlar and Smith[9] among others. Acarlar and Smith show that hairpin shaped vortices were shed by the hemisphere when the flow transitioned and these structures broke down into secondary structures as they moved downstream. Note that such hairpin shaped structures have commonly been observed in turbulent boundary layers by various researchers.[10, 11] Tani[6] studied the effect of Re_k and showed that increasing Re_k beyond a critical value moves the transition location closer to the roughness. Tani suggests that the deformation of the velocity field due to the streamwise vortices (observed even at sub-critical Re_k) shed on the sides of the hemisphere is likely to account for the critical behavior of transition.

A comprehensive review of the effects of roughness on hypersonic boundary layers can be found in Schneider.[3] Some of the suggested mechanisms for hypersonic boundary layers include the concave-wall Gortler instability,[12] the first- and second-mode streamwise-instability described by Mack,[13] the 3-D crossflow instability,[14] and transient growth.[15] As the height of the roughness elements approaches the order of the boundary layer thickness, linear stability analysis of the incoming laminar boundary layer becomes questionable. Chang and Choudhari[16] numerically studied the effect of large roughness elements using a compressible Navier-Stokes code based on the space-time conservation element, solution element (CESE) method. They studied flow past rectangular and cylindrical elements at Mach numbers of 4.1 and 6.5. They concluded that for these Mach numbers, no self-sustained vortex generation was present. They also performed a 2D parametric study and found that at subcritical Reynolds numbers of the boundary layers, absolute instability resulting in vortex shedding downstream was likely to weaken at supersonic free-stream conditions and conjectured that convective instability might be the dominant instability mechanism for supersonic boundary layers. They also observed mushroom shaped streamwise velocity contours in the wake which give rise to inflexion points for the flow downstream of a rectangular fence and a cylindrical shaped roughness.

Danehy et al.[2, 17] studied hemispherical, triangular and rectangular boundary-layer trips placed in supersonic and hypersonic flow over a flat plate using Planar laser-induced fluorescence(PLIF). They observed that at higher Mach numbers, the impact of the roughness element was lower and the flow remained steady. At lower Mach numbers, unsteady structures were observed downstream of the roughness element indicating that the flow was either transitional or turbulent. Also, the onset of transition occurred closer to the roughness element for lower Mach numbers. Bartkowicz et al.[18] studied the effect of a cylindrical protuberance on a Mach 6 laminar boundary layer using DNS. They observed that the vortex system formed upstream of the cylinder resembles the set of vortices seen in incompressible flow by Baker[19] and concluded that for thinner boundary layers, the shock created by the roughness produces a jet of high momentum fluid that recirculates into the vortex system which could cause unsteadiness. Wheaton et al.[20] performed experiments in the Purdue Mach 6 Tunnel and measured the dominant frequency of the disturbance created by the roughness. Redford et al.[21] proposed a correlation for predicting transition induced by a three dimensional roughness element at high-speeds. Marxen and Iaccarino[23] studied a Mach 4.8 flow past a 2D roughness using a body fitted grid and immersed boundary technique. They found that the roughness considerable alters the stability characteristics of the flow although far downstream the stability characteristics resemble that of a flat plate boundary layer. Groskopf et al.[24] performed a bi-global stability analysis of the region downstream of a 3D pizza box shaped roughness and found that the inner pair of counter-rotating vortices caused a pronounced convective instability. They also find that horseshoe vortices don't substantially alter the stability characteristics.

Iyer et al.[22] simulated the flow past an isolated hemispherical bump at conditions that match Danehy et al.[2] and a sinusoidally varying distributed roughness using DNS and found reasonable qualitative agreement with experiment. The distributed roughness produced a fully developed turbulent boundary layer which showed good agreement with existing experimental data at the conditions simulated. They also proposed that a local Reynolds number computed based on the properties at the wall correlates well with the tendency of the flow to transition. Bathel et al.[1] applied a new Nitric-oxide(NO) molecular tagging velocimetry(MTV) technique to obtain averaged axial velocity profiles in the NASA Langley's 31-Inch Mach 10 Air Tunnel for a unit Reynolds number of 1.7 and 3 million/m. They reported velocimetry data for the laminar flowfield downstream of a cylindrical and DTO trips. In this paper, we validate our data for the cylindrical trip case with the above experimental data.

American Institute of Aeronautics and Astronautics

This paper uses DNS to simulate the flow past (I) an isolated cylindrical trip at Mach 8.12, (II) an isolated hemispherical bump on Mach 3.37, 5.26 and 8.23 boundary layer and (III) distributed roughness on a Mach 2.9 boundary layer. The cylindrical trip simulations are performed at conditions that match the experiments by Bathel *et al.*[1] while the hemispherical bump simulations match those in Danehy *et al.*[2] We use a novel algorithm developed by Park & Mahesh[25] to simulate compressible flows on unstructured grids. It employs a modified least–squares approach to reconstruct the fluxes at cell faces (that makes the convective flux computation more accurate), and a scheme to split the viscous stress tensor into the compressible and the incompressible parts (that makes the viscous flux computation accurate). A characteristic filter based shock capturing scheme provides stable solutions in the presence of discontinuities.

The algorithm is described in Section II followed by a brief description of the problem for all three roughness cases in Section III. Sections IV.A and IV.B discuss the results for isolated roughness. The validation of the code using axial velocity profiles from experiment is shown for the cylindrical roughness case and a qualitative description of the transition process for the hemisphere case is discussed. Section IV.C discusses the effect of distributed roughness on the incoming laminar flowfield along with the nature of the flow downstream.

II.   Governing Equations and Numerical Details

The algorithm solves the compressible Navier-Stokes equations on unstructured grids. The governing equations are

$$
\begin{aligned}
\frac{\partial \rho}{\partial t} &= -\frac{\partial}{\partial x_k}\left(\rho u_k\right), \\
\frac{\partial \rho u_i}{\partial t} &= -\frac{\partial}{\partial x_k}\left(\rho u_i u_k + p\delta_{ik} - \sigma_{ik}\right), \\
\frac{\partial E_T}{\partial t} &= -\frac{\partial}{\partial x_k}\left\{\left(E_T + p\right)u_k - \sigma_{ik}u_i - Q_k\right\},
\end{aligned}
\tag{1}
$$

where ρ, u_i, p and E_T are density, velocity, pressure and total energy, respectively. The viscous stress σ_{ij} and heat flux Q_i are given by

$$
\sigma_{ij} = \frac{\mu}{Re}\left(\frac{\partial u_i}{\partial x_j} + \frac{\partial u_j}{\partial x_i} - \frac{2}{3}\frac{\partial u_k}{\partial x_k}\delta_{ij}\right),
\tag{2}
$$

$$
Q_i = \frac{\mu}{(\gamma-1)M_\infty^2 RePr}\frac{\partial T}{\partial x_i}
\tag{3}
$$

after standard non-dimensionalization, where Re, M_∞ and Pr denote the Reynolds, Mach and Prandtl numbers.

The governing equations are discretized using a cell–centered finite volume scheme. Upon integration over the control volume, application of the Gauss theorem and some rearrangement, the governing equations may be written as

$$
\begin{aligned}
\frac{\partial \rho_{\mathrm{cv}}}{\partial t} &= -\frac{1}{V_{\mathrm{cv}}}\sum_{\mathrm{faces}}\rho_f v_N A_f, \\
\frac{\partial \left(\rho u_i\right)_{\mathrm{cv}}}{\partial t} &= -\frac{1}{V_{\mathrm{cv}}}\sum_{\mathrm{faces}}\left[\left(\rho u_i\right)_f v_N + p_f n_i - \sigma_{ik,f}n_k\right]A_f, \\
\frac{\partial \left(E_T\right)_{\mathrm{cv}}}{\partial t} &= -\frac{1}{V_{\mathrm{cv}}}\sum_{\mathrm{faces}}\left[\left(E_T + p\right)_f v_N - \sigma_{ik,f}u_{i,f}n_k - Q_{k,f}n_k\right]A_f,
\end{aligned}
\tag{4}
$$

where V_{cv} is the volume of CV, A_f is the area of the face, n_i is the outward normal vector at surface, and v_N is the face-normal velocity. $\mathbf{q}_{\mathrm{cv}} = \left(\int_{\mathrm{cv}}\mathbf{q}dV\right)/V_{\mathrm{cv}}$ is the volume average within the cell, where $\mathbf{q} = (\rho, \rho u_i, E_T)$ are the conservative variables. Here, the subscript f denotes interpolation at each face of the control volume. The simulations employ a modified least–square method[25] for face reconstruction, which is more accurate than a simple symmetric reconstruction, and more stable than a least–square reconstruction. The algorithm

American Institute of Aeronautics and Astronautics

uses a novel shock–capturing scheme that localizes numerical dissipation to the vicinity of flow discontinuities. The solution is advanced in time using a second–order explicit Adams–Bashforth scheme, as

$$q_j^{n+1} = q_j^n + \frac{\Delta t}{2} \left[3\text{rhs}_j(\mathbf{q}^n) - \text{rhs}_j(\mathbf{q}^{n-1}) \right], \tag{5}$$

where rhs_j denotes j th component of r.h.s. of Eq. (4), and superscript n denotes the n th time step. The algorithm has been validated for a variety of simple problems, as presented by Park and Mahesh.[25]

III. Problem description

Roughness type	M_∞	Re_k	k/δ	T_∞
cylinder	8.12	9406	0.64	73
hemisphere	3.37	9121	2.54	340 K
	5.26	14190	2.08	162.9 K
	8.23	16831	1.19	73K
distributed	2.9	4763	0.35	164K

Table 1. Parameters used in the simulation

III.A. Flow past isolated cylindrical roughness

The simulation parameters match the experiments carried out by Danehy *et al.*[2] in the 31-Inch Mach 10 Air Tunnel at NASA Langley Research Center corresponding to a free-stream unit Reynolds number of 1.7×10^6/m and Mach number of 8.1. The cylindrical trip is 2 mm tall with a diameter of 4 mm. Other parameters are reported in Table 1. Note that the trip is smaller than the boundary layer thickness at its location in the absence of the trip. A compressible similarity inflow is prescribed at the inflow. The computational domain is similar to Figure 2. The computational domain extends from $x=-10$ to 25, $y=0$ to 10 and $z=-20$ to 20 all non-dimensionalized with respect to the diameter of the trip. The trip is located at $x=0$. The computational domain is longer than the experimental setup in both downstream distance and spanwise width. An isothermal wall condition with $T_{wall}=300$K is prescribed. The grid is composed of 13 million hexahedral elements.
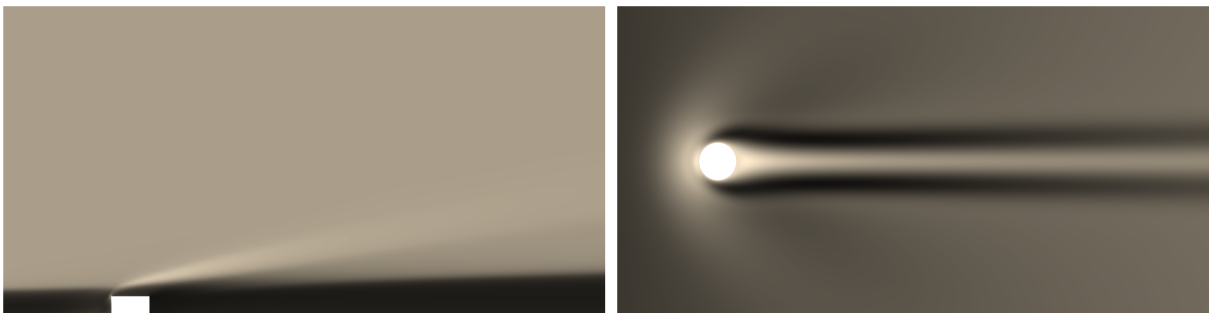

Figure 1. Instantaneous density contours in symmetry plane(left) and instantaneous streamwise velocity contours on a wall normal plane 0.2 diameters from the wall(right) for flow past cylinder.

Figure 1 shows the instantaneous density contours of the flow in symmetry plane on the left and instantaneous streamwise velocity contours on a plane 0.2 diameters from the wall on the right. The flow downstream remains laminar and does not transition as can be seen from the instantaneous velocity contours on the right. Note the shock produced by the roughness and coherent streamwise vortices causing high speed streaks downstream of the cylindrical roughness in Figure 1. From the symmetry plane contour, it can also be seen that the boundary layer thickness is greater than the height of the roughness. This case was simulated for validating the velocity profiles obtained from the experiments by Bathel *et al.*[1]

American Institute of Aeronautics and Astronautics

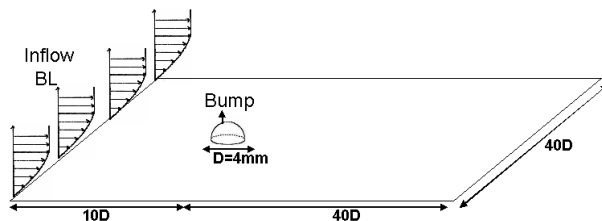## III.B. Flow past isolated hemispherical roughness

Figure 2. Schematic of the flow past an isolated hemispherical roughness element.

The parameters match those in the experiments of Danehy *et al.*[2] The unit Reynolds number is 6.1 million/m. In the experiment, a Mach 10 flow is incident on a 20° full angle wedge placed at different angles to the flow ranging from 5 to 25. The top surface of the wedge is modeled as a flat plate with the post-shock conditions at the leading edge taken to be the free-stream conditions. We simulate the lowest, intermediate and highest Mach number corresponding to wedge angles of 25°, 15° and 5°. The free-stream conditions were calculated using theoretical oblique shock relations and also verified with the experimentally measured conditions. The resulting free-stream conditions are shown in Table 1. The Reynolds number is calculated based on the diameter of the hemisphere which is 4 mm. All length scales are non-dimensionalized with respect to the diameter of the hemisphere and the non-dimensional free-stream velocity and density is taken as unity. The grid is composed of 40 million hexahedral elements. Additional details about the grid can be found in Iyer *et al.*[22] A schematic of the computational domain is shown in Figure 2. The computational domain extends from -25 to 25 units in the streamwise direction, -20 to 20 units in the spanwise direction and -10 to 10 units in the wall normal direction. The hemisphere is located at $x=-15$ (10 units downstream of the inflow). A compressible similarity solution at conditions corresponding to a streamwise distance of 8.85 units is prescribed at the inflow. An isothermal wall condition with $\text{T}_{wall}=300\text{K}$ is prescribed for all the three Mach numbers simulated.
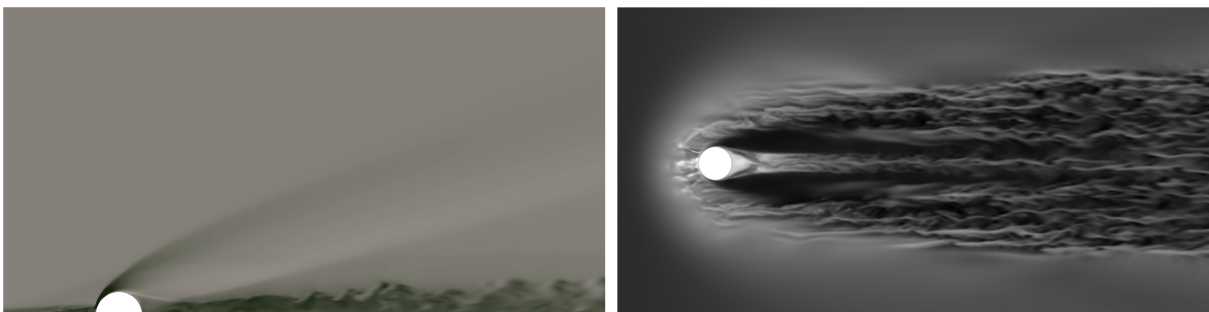

Figure 3. Instantaneous temperature contours in symmetry plane(left) and instantaneous streamwise velocity contours on a wall normal plane 0.1 diameters from the wall(right) for flow past hemispherical bump for $M_\infty=3.37$.

Figure 3 shows instantaneous temperature contours of the flow for $M_\infty=3.37$ in the symmetry plane on the left and instantaneous streamwise velocity contours at a plane 0.1 diameters from the wall on the right. Note the shock produced by the roughness and coherent streamwise vortices causing high speed streaks which breakdown downstream of the roughness in Figure 3. The symmetry plane contours show that the boundary layer thickness is lower than the height of the roughness. Unsteady flow features can also be observed in the symmetry plane downstream of the roughness. Low velocity regions upstream of the roughness in the wall normal plane show the bow shock produced.

III.C. Flow past distributed roughness

Direct numerical simulations of supersonic flow (Mach 2.9) past a flat plate with a distributed roughness were performed. Figure 4 shows snapshots from this simulation. Note that only a portion of the computational domain is shown. The streamwise and spanwise directions are x and z respectively. Incoming laminar flow

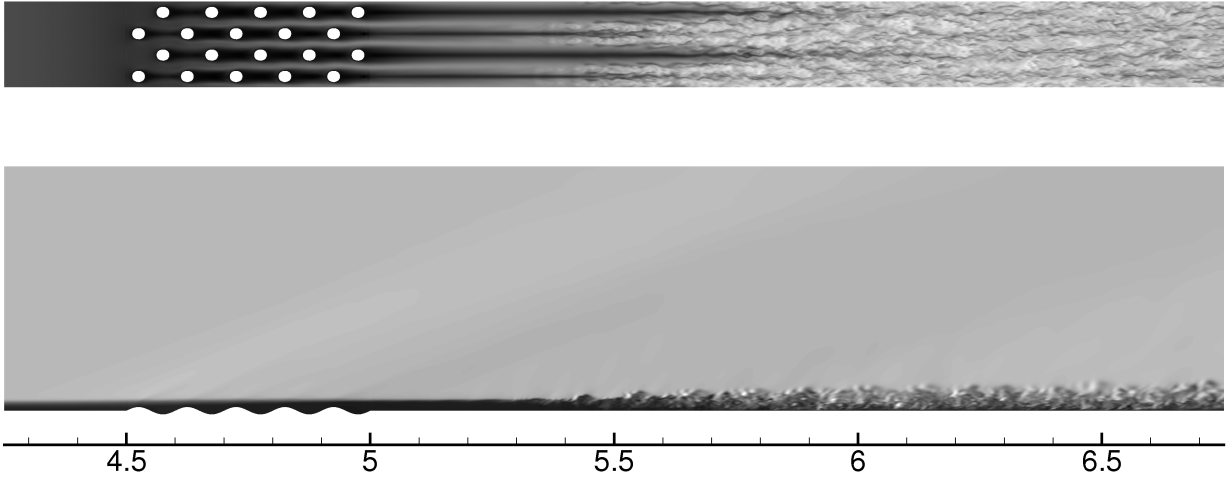American Institute of Aeronautics and Astronautics

Figure 4. Figure shows snapshots from simulation of laminar flow past distributed roughness elements. Top view shows contours of velocity while the side view shows contours of density.

(inflow at $x = 4.0$) at Mach 2.9 encounters a roughness strip between x=4.5 and x=5.0 inch. Roughness is prescribed as $y_{wall} = h sin(k_1 x) sin(k_2 y)$ where h is 0.0075 inch, and the roughness spans two wavelengths in the span and five wavelengths in the streamwise direction. The unit Reynolds number is 635000 (/per inch). Isothermal boundary conditions are applied at the wall, with the wall temperature set to be the adiabatic temperature at Mach 2.9. The computational mesh consists of roughly 36 million hexahedral elements. The mesh spacing is uniform in the streamwise and spanwise directions and clustered in the wall–normal direction such that the elements closest to the wall have the smallest Δy. The mesh sizes are : $\Delta x = 2.5 \times 10^{-3}$, $\Delta z = 91 \times 10^{-4}$, and $\Delta y_{min} = 5 \times 10^{-5}$.

IV.   Results

IV.A.   Flow past isolated cylindrical roughness

Velocity profiles in the spanwise symmetry plane are compared to the experiments at different streamwise locations in Figure 5. The experiment uses a Nitric Oxide (NO) molecular tagging velocimetry (MTV) technique to obtain averaged axial velocity. An interline, progressive scan CCD camera was used to obtain separate images of the initial reference and shifted NO molecules that had been tagged by the laser. Further details of the experiment can be found in Bathel *et al.*[1] Note that the center of the trip is at x=7.54 cm. The error bars in the figure indicate experimental uncertainty as provided by Danehy.[26] Profiles at streamwise locations very close to the roughness are not shown due to the large uncertainty at these locations. Reasonable agreement is found between the computation and experiment. At x=5.01 cm, it can be seen that the profile resembles that of a 2D laminar boundary layer. At x=7.86 cm, a strong inflexion point in the $u - y$ profile is observed which affects the stability characteristics of the flow. With increasing distance downstream of the roughness, the inflexion point becomes weaker and the profile tends towards a 2D laminar boundary layer profile.

Velocity profiles at a wall normal plane 2.1 mm from the wall are compared to experiment at different streamwise locations in Figure 6. A difference of the order of 100 m/s is observed between the computed and experimental data upstream of the roughness. This difference is attributed to the 0.5 mm uncertainty in the laser position in the experiment.[26] Downstream of the roughness, reasonable agreement is observed. For the particular experimental technique used, it can be seen in the symmetry plane profiles that the uncertainty values increase with increasing distance from the wall. The profiles downstream of the roughness can be seen to have a wake-type profile close to the symmetry plane with a peak on the either side due to the acceleration of the flow around the roughness.
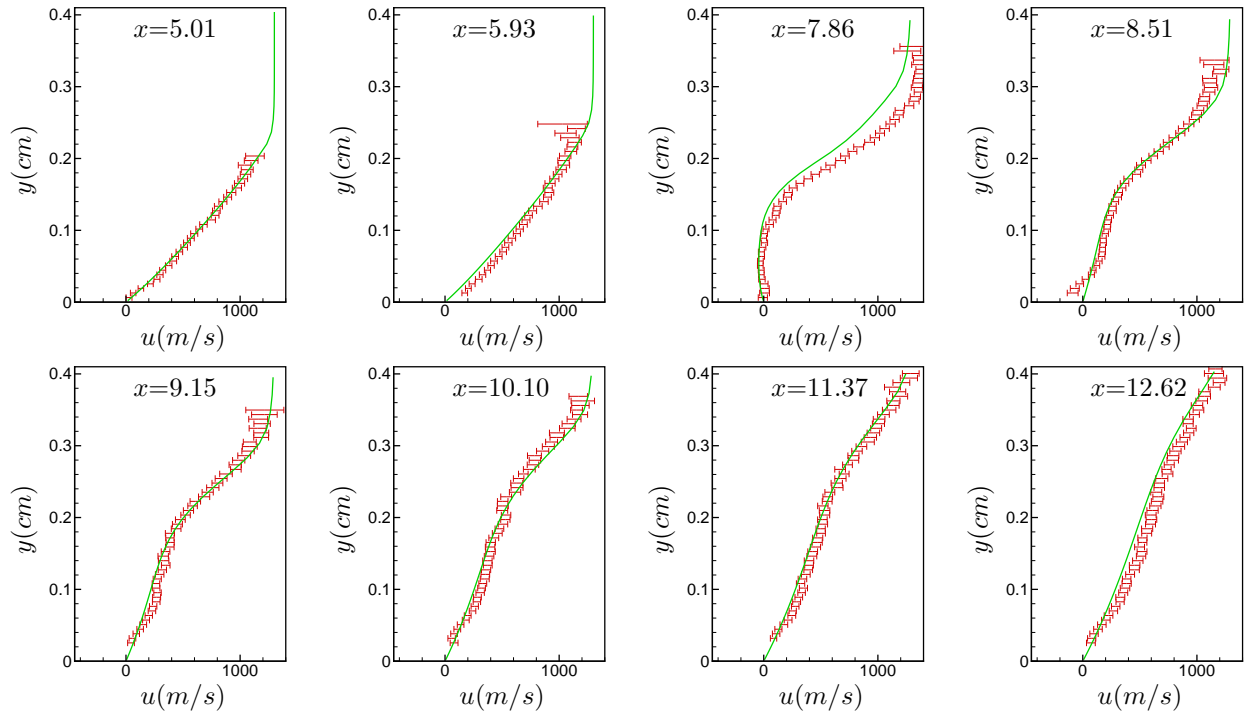
American Institute of Aeronautics and Astronautics

Figure 5. Symmetry plane streamwise velocity profiles at different stations compared with experiments by Bathel *et al.*[1] Streamwise locations in cm.
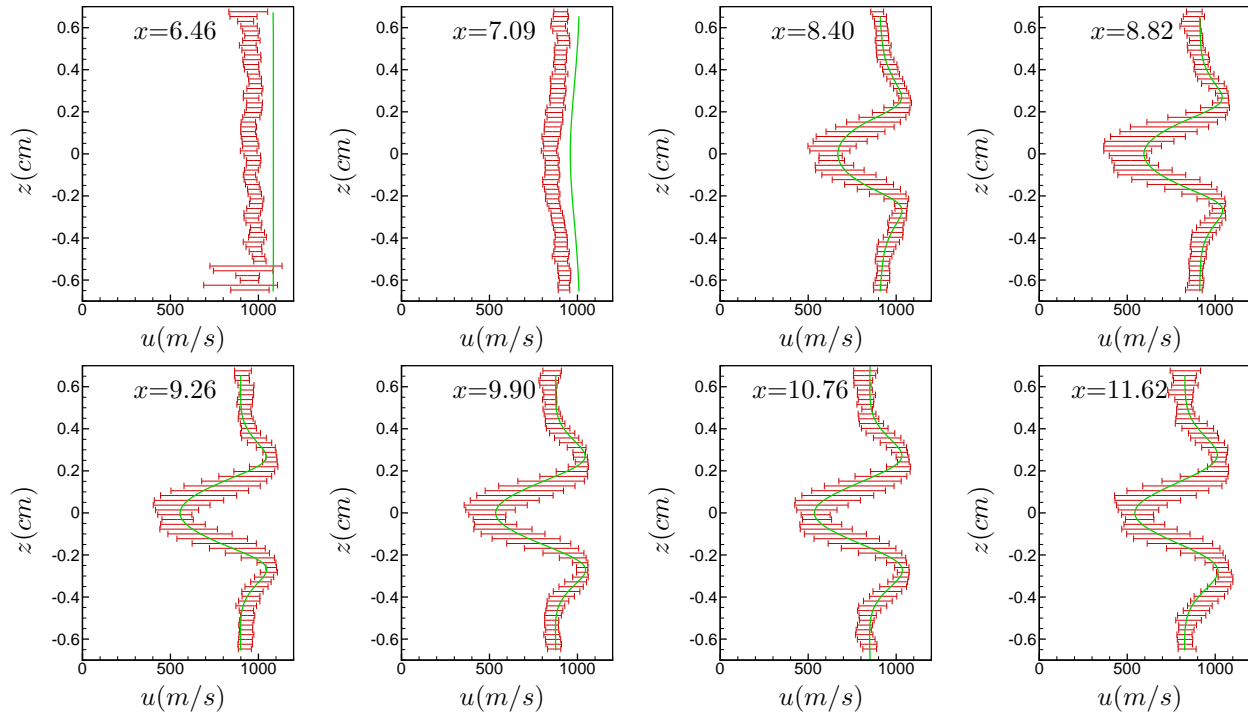

Figure 6. Wall normal plane streamwise velocity profiles at different stations 2.1 mm above the flat plate compared with experiments by Bathel *et al.*[1] Streamwise locations in cm.

IV.B. Flow past isolated hemispherical roughness

Flow past a hemispherical bump is simulated at three Mach numbers. The observations made in our earlier study[22] that the flow downstream of the roughness transitioned for the lower Mach number cases and

remained laminar for the highest Mach number case is in agreement with the experimental observations by Danehy *et al.*[2] A qualitative description of the transition process follows. A boundary layer separates ahead of an obstruction, producing a system of vortices. Figure 7 shows the streamlines on the symmetry plane upstream of the bump depicting the system of vortices formed due to the separation of the boundary layer. It can seen in Figure 7 that very close to the corner between the hemisphere and flat plate, a counter-clockwise rotating vortex is present while three clockwise rotating vortices can be observed closer to the separation streamline. These vortices wrap around the roughness producing necklace shaped vortices. The wrapping of the upstream vortex system around the roughness is shown in Figure 8 where an isocontour of Q-criterion with streamwise vorticity contours is plotted. In the figure, red and blue colors indicate clockwise and counter-clockwise directions of rotation respectively in a streamwise plane while looking in the direction of the flow. It can be seen that a pair of counter-rotating streamwise vortices are observed close to the symmetry plane and away from the symmetry plane on either side. A schematic of these vortices is shown in Figure 8 at the center of the roughness with the direction of flow towards the observer. Symmetry plane (SP) vortices move closer to each other as they move downstream forming a counter-rotating pair of vortices. The movement of the SP vortices is both a result of the mean spanwise velocity and the inviscid induced velocity generated by the image vortices due to wall effects. Off-symmetry plane (OSP) vortices are produced due to the wrapping of upstream vortex system and one counter-rotating pair of vortices are formed on either side of the roughness.
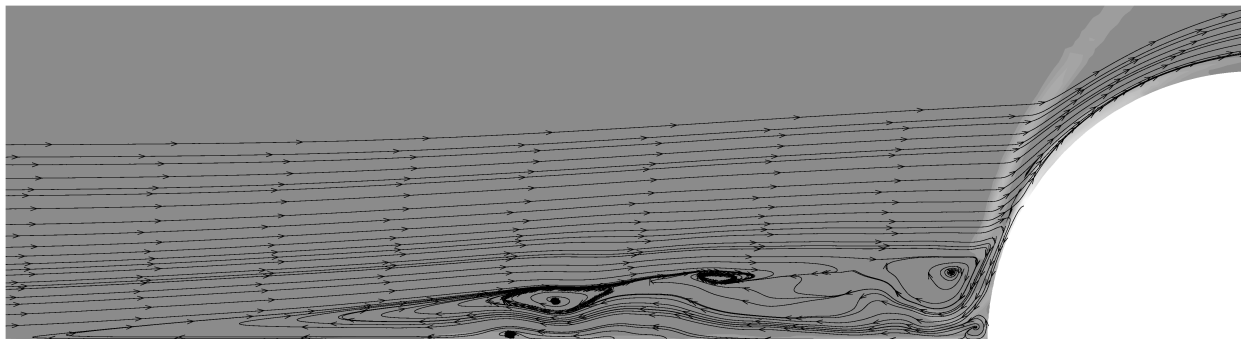

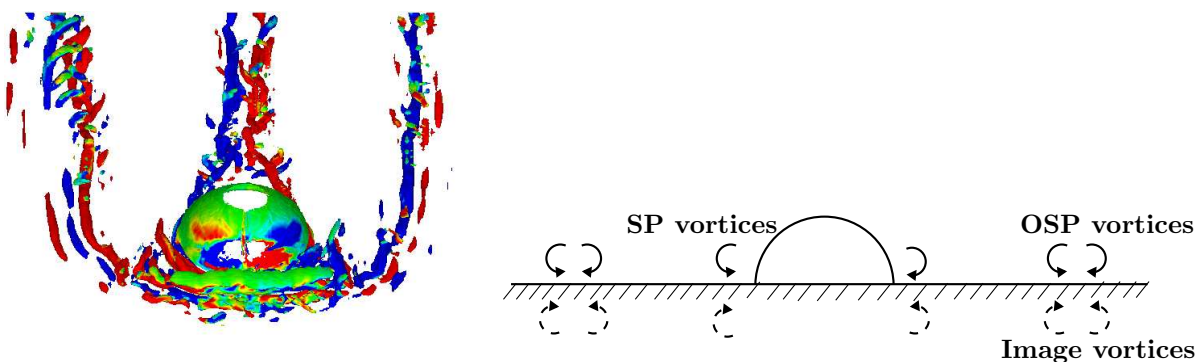Figure 7. Streamlines showing system of vortices formed upstream of bump for M_∞=3.37.

Figure 8. Isocontour of Q-criterion showing the wrapping around of upstream vortices(left) and a schematic of the vortex system in a streamwise plane at the center of roughness(right) for M_∞=3.37.

Streamwise vortices transport higher momentum fluid from above closer to the wall and push lower momentum fluid upwards. This produces high-speed streaks in a plane very close to the wall and low-speed streaks away from the wall. Thus, the skin friction coefficient at the wall increases in regions close to the streamwise vortices. Figure 9 shows the mean streamwise velocity contours at a plane 0.1D above the flat plate for the three Mach number cases with blue indicating higher velocity. For the lower Mach number cases, we see that both the SP and OSP vortices are dominant whereas for M_∞=8.23, we see that only the SP vortices are dominant. It can also be seen that for M_∞=8.23, the strength of the vortices decays with downstream distance while for the lower Mach number cases, the vortices appear coherent until a
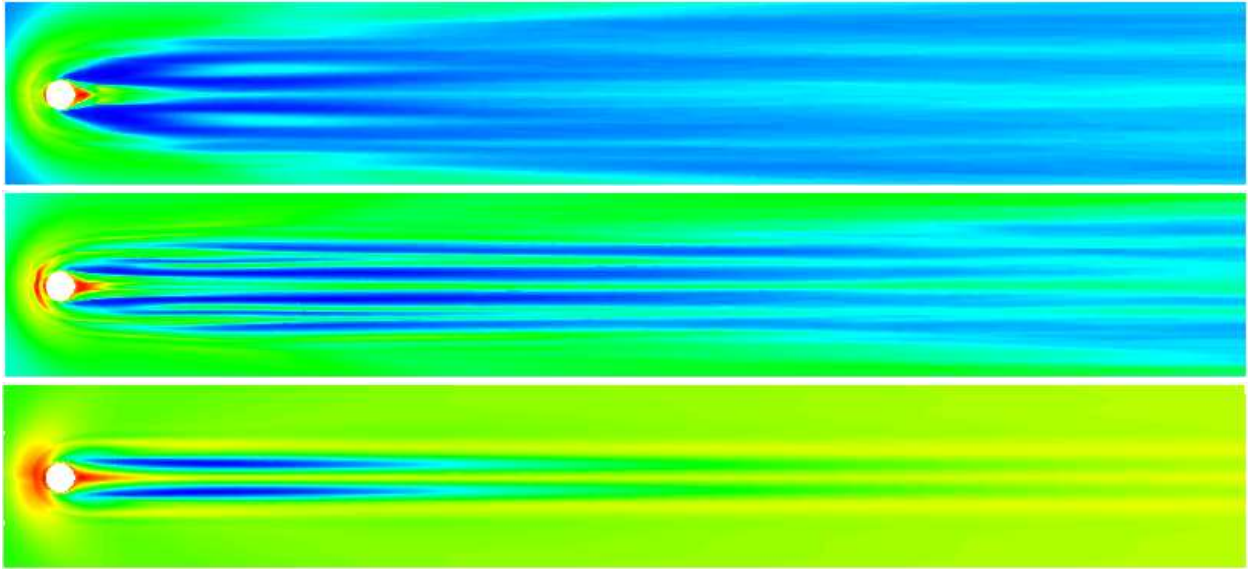
American Institute of Aeronautics and Astronautics

Figure 9. Mean streamwise velocity contours at 0.1D from the wall for M_∞=3.37(top), M_∞=5.26(center) and M_∞=8.23(bottom).
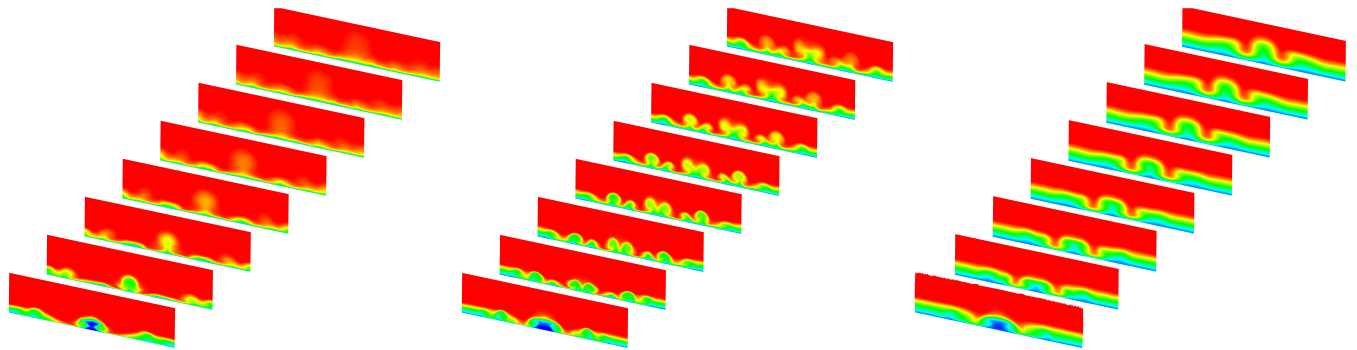

Figure 10. Streamwise planes showing evolution of the mean streamwise velocity for M_∞=3.37(left), M_∞=5.26(center) and M_∞=8.23(right).

point beyond which they breakdown and significant spanwise mixing of the flow is observed. Note that the coherent streamwise vortices breakdown closer to the bump for M_∞=3.37 as compared to M_∞=5.26. Also, the spacing between the SP vortices is lowest for M_∞=3.37 at this location as compared to M_∞=5.26 and 8.23.

The wall–normal transport of momentum by the streamwise vortices yields 'mushroom–shaped' velocity contours in the crossplanes (figure 10). Similar behavior has been observed by Choudhari *et al.*[16] Figure 10 shows the evolution of mean streamwise velocity with downstream distance from the bump for three Mach numbers. The planes are located at equally spaced downstream distances of 1 to 15 diameters from the bump with the spanwise extent of the plane being 4 diameters and height equal to 1 diameter. It is apparent that such velocity contours correspond to spanwise and wall–normal inflexional profiles.

Figure 11 shows the iso-contour of Q-criterion plotted with the streamwise velocity for M_∞=3.37 case. Hairpin shaped structures are observed. Similar hairpin shaped structures were observed for M_∞=5.26 case but no such structures were observed for the M_∞=8.23 case. We also observe that hairpins are produced at locations which correspond to those of the counter-rotating vortex pair showing that the breakdown of streamwise vortices, and therefore transition is related to the formation of hairpins. As discussed in Section IV.C, hairpin shaped structures are also observed in the flow that transitioned due to distributed roughness.

Figure 12 shows the mean C_f variation with streamwise distance at an off-symmetry plane for the three Mach numbers. The profiles are plotted at a distance of 1 diameter for the lower Mach number cases and
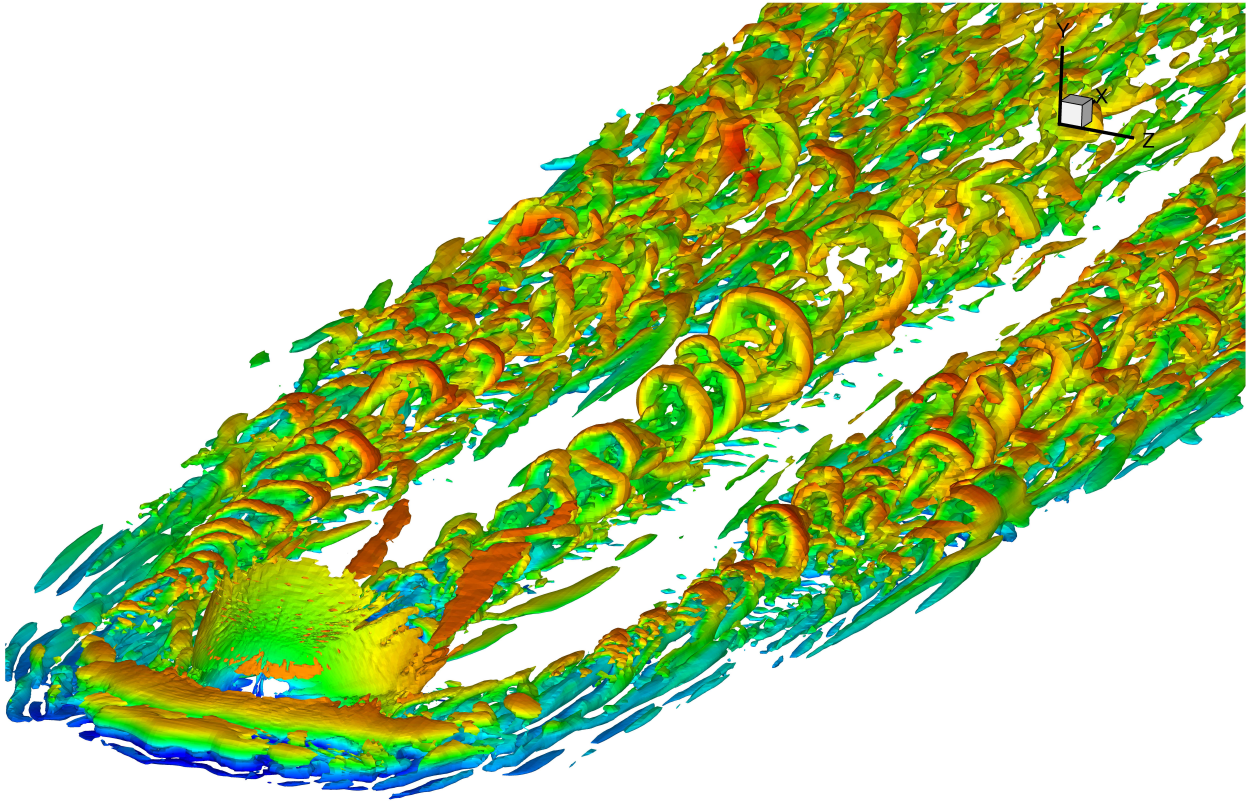
American Institute of Aeronautics and Astronautics

Figure 11. Iso-contour of Q-criterion for M_∞=3.37 with streamwise velocity contours showing hairpin structures.

0.5 diameter for M_∞=8.23 from the symmetry plane. The roughness is located at x=−15. It was seen in Iyer *et al.*[22] that the C_f upstream of the bump matched that of a 2D laminar boundary layer. Immediately downstream of the roughness, there is a significant rise in C_f for all the three cases. It is important to note that even for a case where the flow does not transition, the C_f could be substantially higher than the laminar value for a reasonable distance downstream of the roughness due to the presence of streamwise vortices. Far downstream, the curves indicate that the lower Mach number cases transition whereas M_∞=8.23 remains laminar which is consistent with the experimental observations.

Figure 13 shows the Van Driest transformed velocities for all three cases at four spanwise locations of 0.25, 0.5, 1 and 2 diameters from the symmetry plane and 25 diameters downstream of the bump. The profiles for M_∞=8.23 indicate the laminar nature of the flow consistent with earlier observations. M_∞=3.37 profiles show that the flow is well mixed in the spanwise direction causing the different profiles to collapse into one curve. We also see that the flow is not a fully developed turbulent boundary layer in that the log law is not satisfied. For M_∞=5.26, we see that there is spanwise variation in the velocity at this downstream location which is consistent with the observations in Figure 9.

Figure 14 shows the variation of the root mean square of the velocity fluctuations normalized with the free-stream velocity at spanwise locations matching those of Figure 12. Note that the trends observed here is consistent with the C_f curves in Figure 12. For M_∞=3.37, the rms of velocity fluctuations rises to a peak of 0.18 downstream of the roughness beyond which it settles down close to a value of 0.12. For M_∞=5.26, the rms value rises almost monotonically to the peak value of around 0.15 and maintains the value further downstream. For M_∞=8.23, although small in magnitude, we observe unsteadiness downstream of the roughness until x=10 beyond which the flow becomes steady. Note that for all the three cases, unsteadiness is produced upstream of the roughness indicated by peaks in the rms curves.
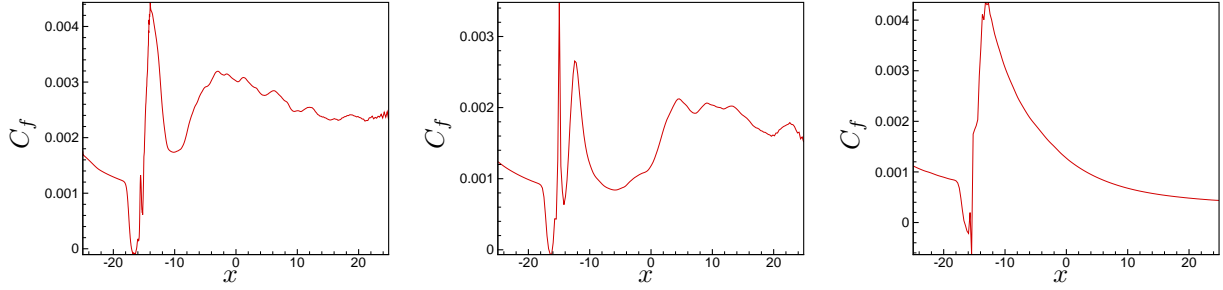
American Institute of Aeronautics and Astronautics

Figure 12. Skin friction coefficient variation with streamwise distance in an off-symmetry plane for M_∞=3.37(left), M_∞=5.26(center) and M_∞=8.23(right).
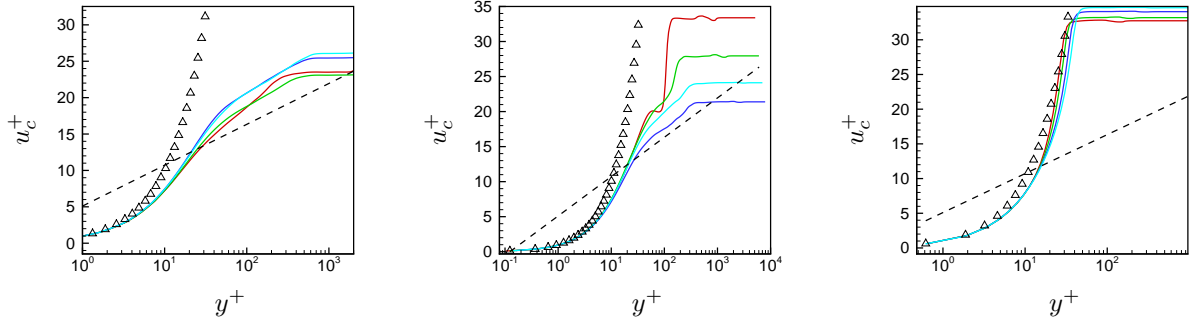

Figure 13. Van Driest transformed velocity at different spanwise locations at 25 diameters downstream of the bump for M_∞=3.37(left), M_∞=5.26(center) and M_∞=8.23(right).
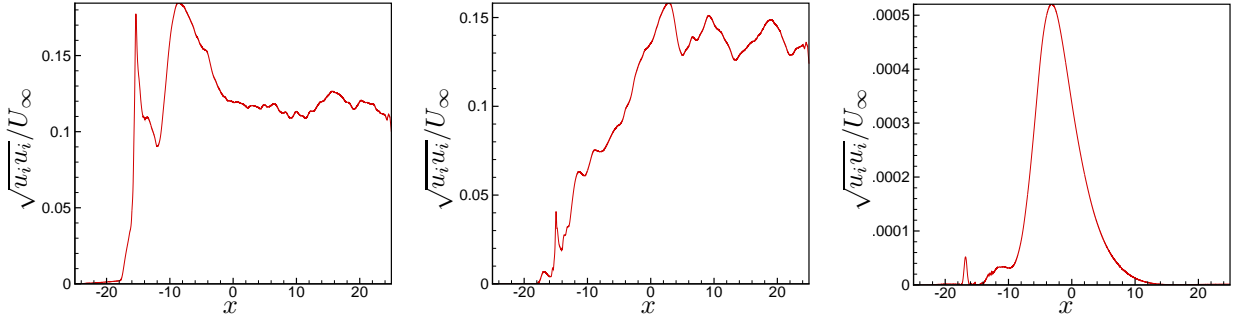

Figure 14. Streamwise variation of RMS of velocity fluctuations at off symmetry planes for M_∞=3.37(left), M_∞=5.26(center) and M_∞=8.23(right).

IV.C. Flow past distributed roughness

The distributed roughness shown in Figure 4 perturbs the laminar incoming flow causing it to transition downstream of the roughness strip. The resulting unsteadiness is clearly visible. Figure 15 shows a snapshot of the flow field using isosurfaces of Q criteria, colored by contours of streamwise velocity. Note that only a portion of the streamwise domain is shown. The incoming flow is laminar, steady and two–dimensional, all of the vorticity is ω_z. Roughness modifies the vorticity field, and the figure shows contours that indicate the location of the individual roughness elements. Pairs of streamwise vortices are observed behind the roughness elements, which are followed by highly unsteady flow and a transition to turbulence. Note that multiple hairpins are visible in this snapshot.

Similar to the flow past the single hemispherical element in Section IV.B, we observe deceleration in front of the individual roughness elements, acceleration on the sides, and streamwise vortices behind each of them which appear to break down (further downstream). The consequence of having multiple roughness elements is that these features do not persist long into the downstream: instead, they interact with surrounding
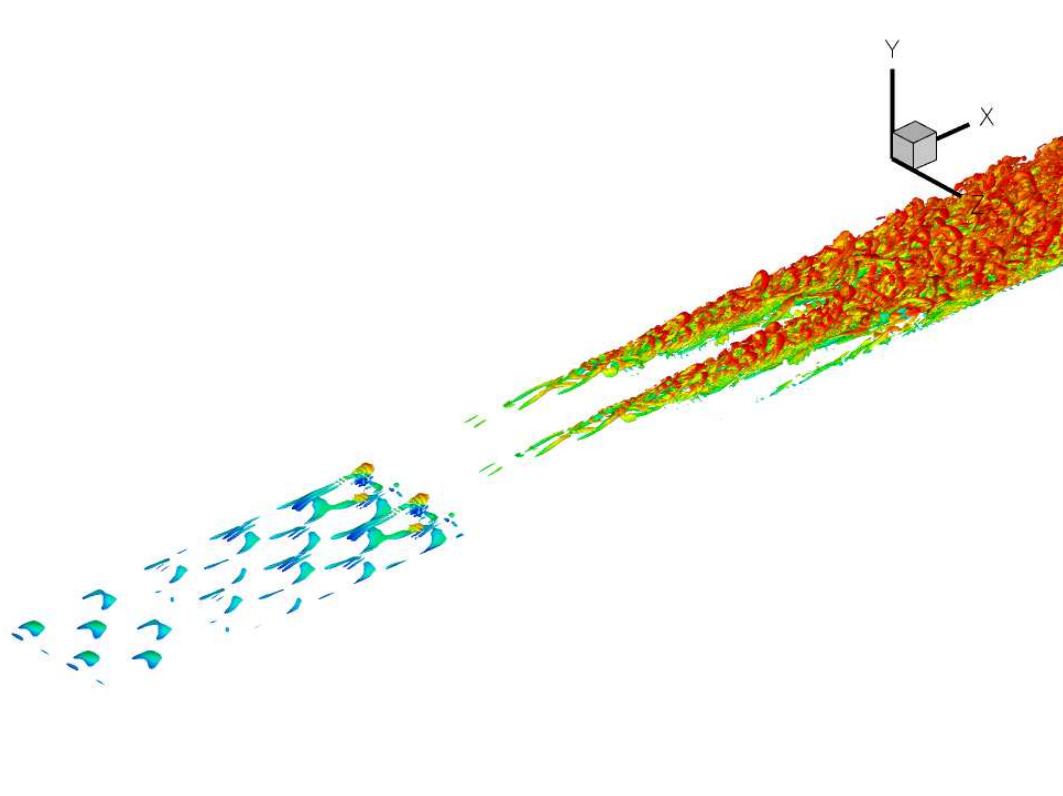
American Institute of Aeronautics and Astronautics

Figure 15. A snapshot of the flow using isocontours of Q criteria (Q = 150) colored by contours of the streamwise velocity.

roughness elements. The cumulative effect of multiple roughness elements is to slow down the flow close to the wall, which appears to breakdown in the smooth wall region downstream of the roughness.

Figure 16 shows the profiles of density, and components of velocity and vorticity at a few spanwise locations, and at a streamwise location corresponding to the first row of roughness elements. These locations in the span correspond to the crests (shown in green), troughs (black) and in between the roughness elements (red, blue). The decrease in the streamwise velocity due to the roughness elements can be observed, along with the change in the density profile at these points (green). There is a small (and symmetric) spanwise velocity w due to the curvature of the roughness elements, and the peak in this profile corresponds to $y \sim$ 0.004, less than the roughness height of 0.0075 inches. At this location, roughness elements push fluid away from the wall, as can be observed by the positive v velocity. This perturbed velocity field also shows non–zero values for ω_x and ω_y, though the magnitudes are lower than that of ω_z.

Figure 16 shows the effect of the first row of roughness elements on the incoming boundary layer. The cumulative effect of the roughness strip can be similarly observed from Figures 17 and 18. Figure 17 shows contours of velocity and vorticity at x=5.0, the end of the roughness strip (and where the flow is not turbulent, according to Figure 4). Directly downstream of the roughness elements, the figure shows low streamwise velocity region (wake), and regions of significant vorticity field. All the contours show spanwise variations, indicating that the roughness-perturbed flow is now three–dimensional. Contours of ω_x shows the distinct presence of streamwise vortices of alternating orientation (counter–rotating vortices). Qualitatively, the streamwise velocity figure is similar to Figure 10 of the isolated roughness case.

Figure 18 shows vertical profiles of density, and components of velocity and vorticity at x=5.0. u profile shows slower fluid directly behind the roughness elements, and faster fluid in between the roughness elements. Note that this spanwise alternating high and low u velocity is evident from Figure 4. The slow fluid shows (in comparison with Figure 16) increased velocity deficit (due to decelerated fluid behind the roughness elements), and an inflexion point, and the profile bears resemblance to that of a mixing layer. Also, spanwise velocity w and the magnitude of vorticity are higher than in Figure 16. The location of the velocity gradient ($y \sim 0.02$) is higher than the peak roughness height (0.0075) and is closer to the incoming boundary layer thickness ($\delta_{ionflow} \sim 0.022$).
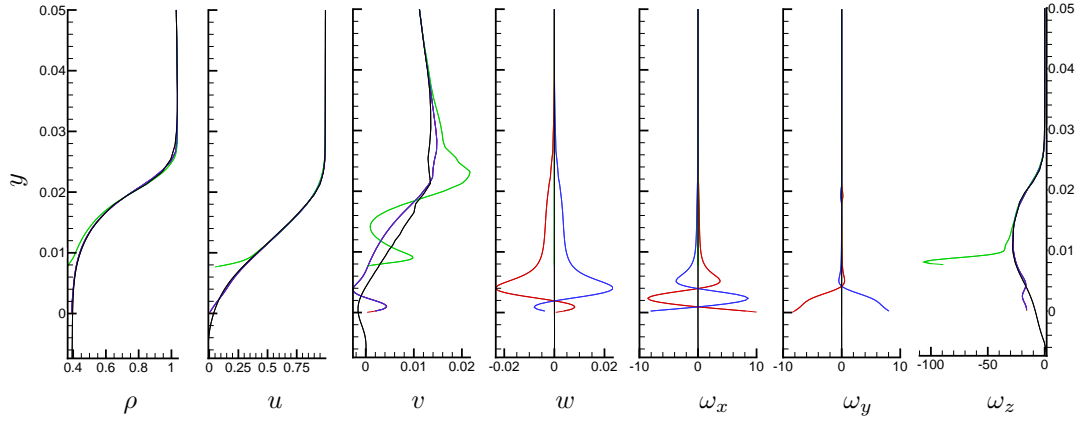
American Institute of Aeronautics and Astronautics

Figure 16. Instantaneous vertical profiles of density, velocity and vorticity at $x=4.525$, location corresponding to the peaks of the first row of roughness elements.
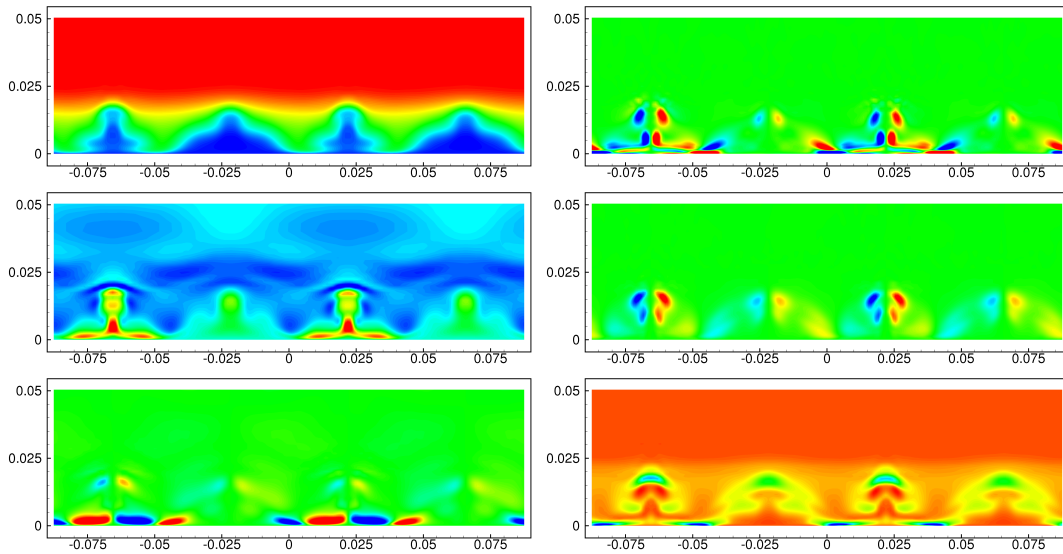

Figure 17. Snapshots of the flow at $x = 5.0$, the end of the roughness strip. Figures show the perturbed velocity and vorticity fields due to the surface roughness. The top row shows contours of u and ω_x, second shows v and ω_y, third shows w and ω_z.
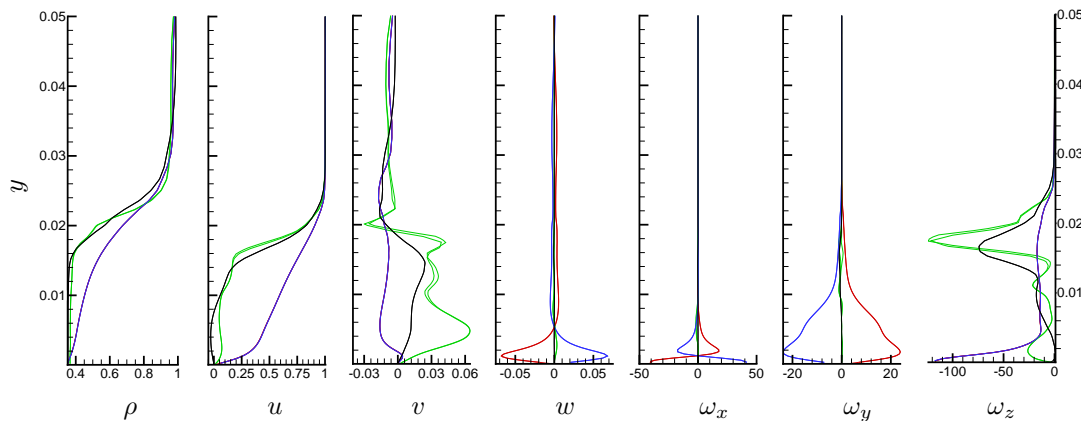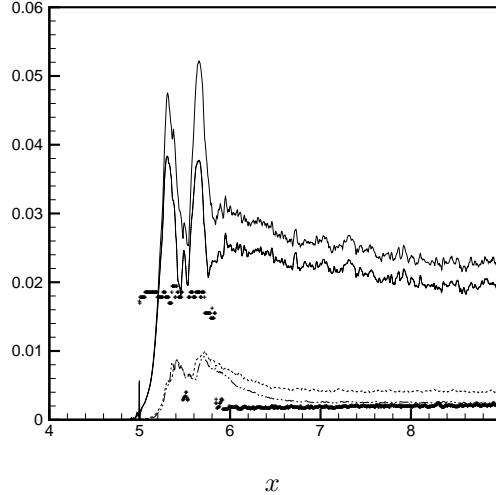

Figure 18. Instantaneous vertical profiles of density, velocity and vorticity downstream of the roughness strip. The colors correspond to the same spanwise stations as Figure 16.

American Institute of Aeronautics and Astronautics

Figure 19. Variation of maximum turbulent intensities as a function of x. ———: $u'_i u'_i$, ········: $u'u'$, —··—: $v'v'$, and ————: $w'w'$. **Symbols show the wall–normal location of the maximum turbulent kinetic energy.**

Figure 19 plots maximum turbulent intensities with the streamwise distance. This figure is an indication of the unsteadiness in the flow in the pre–transition region. There is some unsteadiness by the end of the roughness strip, unsteadiness increases past x=5.0, shows two peaks and steadily decreases there after. Interestingly, peak $v'v'$ and $w'w'$ slightly lag the peak $u'u'$. The figure also shows the y location of the maximum $u'u'$. Between x of 5 and 6, the most unsteadiness is observed in the vicinity of $y \sim 0.02$, which corresponds to the inflexion point and the high velocity gradient observed in figure 18. Post–transition, the peak $u'u'$ is observed much closer to the wall, a feature characteristic of turbulent boundary layers. Note that the two peaks in $u'u'$ correspond to different spanwise locations, and is a feature of this particular (staggered) arrangement of the individual roughness elements. Figure 20 shows snapshots of the flow corresponding to these peak intensities. The instability originating from the inflexion points can be observed, along with the quick transition from unsteady flow to a turbulent flow.

Thus, it appears that the roughness strip causes a slowing down of the fluid close to the wall, resulting in a sharp $\partial u/\partial y$ gradient and an inflexion point. There is also an acceleration of fluid in between the roughness elements, but this fluid appears not to transition before the slower fluid. While the flow near each of the roughness elements bears some direct similarities to the flow past the isolated hemisphere, the cumulative effect of the roughness strip shows differences. In the hemisphere case, the streamwise vortices and their breakdown dominate the flow where as in this case, the dominating effect appears to be due to the deceleration of the fluid close to the wall (close to the roughness elements) and the resulting mixing-layer-like velocity profile.

Transition thus induced gives rise to a flow that is turbulent, and the mean flow characteristics of the turbulent region agree well with existing data at similar conditions. Figure 21(a) presents the variation of skin friction coefficient with Re_θ (based on μ_{wall}), adapted from Loginov et $al.$[27] Note that the present results fall well within the scatter observed among the other experiments/simulations. figure 21(b) shows the variation of streamwise velocity, density, Mach number and temperature across the boundary layer at a few streamwise locations : $x = 6.5, 7, 7.5, 8,$ and 8.5 inches along with experimental (Zheltovodov et $al.$,[28] Bookey et $al.$,[29] Ringuette et $al.$[30]) and simulation (Loginov et $al.$[27]) results. Good agreement is observed.
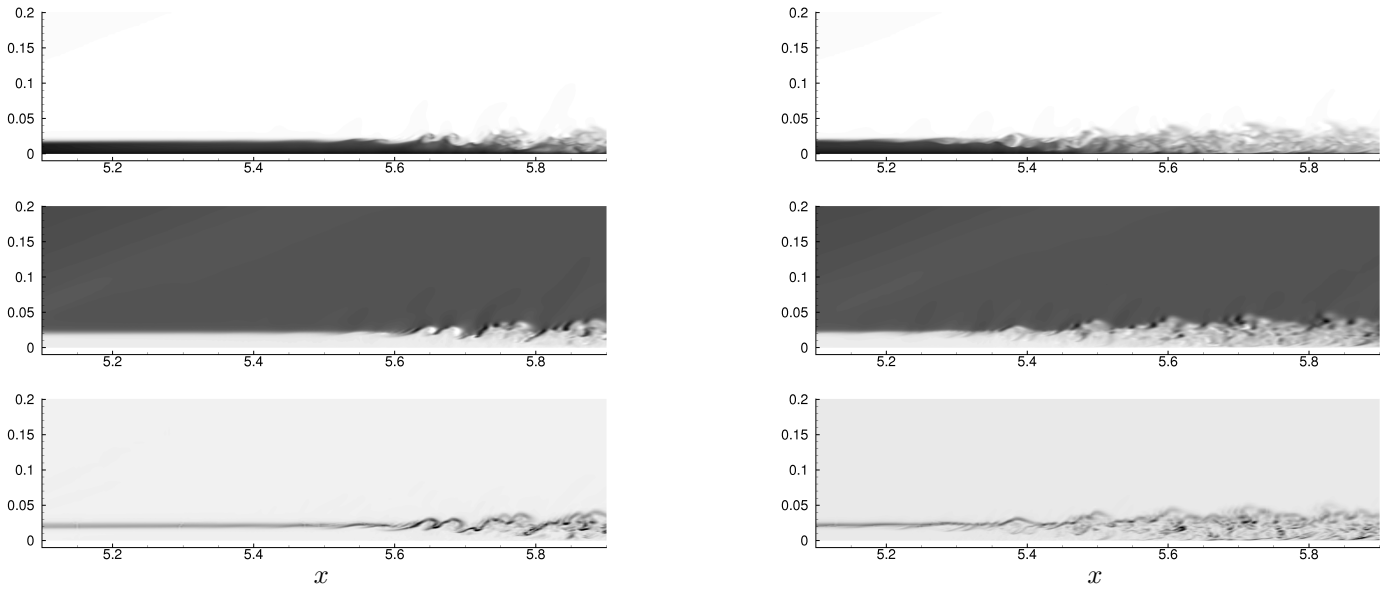
Acknowledgments

Figure 20. Snapshots of the flow at two off-symmetry planes that corresponds to where the peak velocity gradients were seen in figure 18. Contours of (top to bottom) streamwise velocity, density, density gradient. Roll-up features are observed around $y \sim 0.02$.
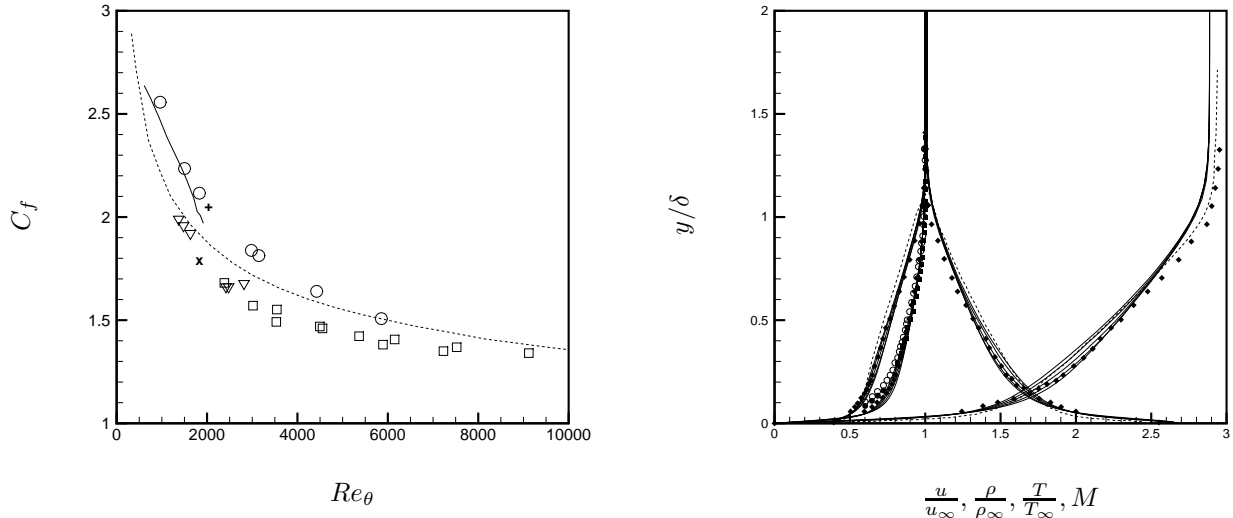

Figure 21. (a) Variation of C_f vs Re_θ from the present simulation (——) and compared to available data obtained from Loginov *et al.*:[27] Vandriest II transformation prediction (– – – –), Loginov *et al.*[27] LES (+), Zheltovodov *et al.*[28] (x), Stalmach Mach 2.78 (○), Mabey *et al.* Mach 3 (□) and Laderman and Demetriades (▽). (b) Comparison of profiles of density, streamwise velocity, Temperature and Mach number across the boundary layer. Profiles from the present DNS correspond to $x = 6.5$, 7. 7.5, 8 and 8.5(——); Loginov *et al.*[27] LES: —·—; symbols from experiments - Bookey *et al.*[29] (■), Zheltovodov *et al.*[28] (♦), and Ringuette *et al.*[30] (●).

American Institute of Aeronautics and Astronautics

References

[1] B. F. Bathel, P. M. Danehy, J. A. Inman, A. N. Watkins, S. B. Jones, W. E. Lipford, K. Z. Goodman, C. B. Ivey & C. P. Goyne, "Hypersonic Laminar Boundary Layer Velocimetry with Discrete Roughness on a Flat Plate", AIAA-2010-4998.

[2] P. M. Danehy, B. Bathel, C. Ivey, J. A. Inman & S. B. Jones, "NO PLIF study of hypersonic transition over a discrete hemispherical roughness element," AIAA 2009-394.

[3] S. P. Schneider, "Effects of Roughness on Hypersonic Boundary-Layer Transition," *Journal of Spacecraft and Rockets*, Vol 45, No. 2, March-April 2008.

[4] E. Reshotko, "Is Re_θ/M_e a Meaningful Transition Criterion?", *AIAA Journal*, Vol. 45, No. 7, July 2007.

[5] D. C. Reda, "Review and Synthesis of Roughness-Dominated Transition Correlations for Reentry Applications", *Journal of Spacecraft and Rockets*, Vol. 39, No. 2, March-April 2002.

[6] I. Tani, H, Komoda & Y. Komatsu, "Boundary-Layer Transition by Isolated Roughness", *Aeronautical Research Institute, University of Tokyo, Report No. 375, November 1962.*

[7] H. L. Dryden, "Review of published data on the effect of roughness on transition from laminar to turbulent flow," *J. Aeronaut. Sci. 20, 477-482(1956).*

[8] P. S. Klebanoff, W. G. Cleveland & K. D. Tidstrom, "On the evolution of a turbulent boundary layer induced by a three-dimensional roughness element", *J. Fluid Mech. (1992), vol. 237, pp. 101-187.*

[9] M. S. Acarlar & C. R. Smith, "A study of hairpin vortices in a laminar boundary layer. Part 1. Hairpin vortices generated by a hemisphere protuberance", *J. Fluid Mech (1987), vol.175, pp. 1-41.*

[10] M. R. Head & P. Bandyopadhyay, "New aspects of turbulent boundary-layer structure", *Journal of fluid mechanics (1981), 107: 297-338.*

[11] R. J. Adrian, "Hairpin vortex organization in wall turbulence", *Phys. Fluids 19, 041301 (2007); doi:10.1063/1.2717527.*

[12] W. S. Saric, "Gortler Vortices," *Annual Review of Fluid Mechanics*, Vol. 26, 1994, pp. 379-409.

[13] L. M . Mack, "Boundary Layer Linear Stability Theory," *Report 709, Special Course on Stability and Transition of Laminar Flow*, AGARD, March 1984, pp. 1-81.

[14] W. S. Saric, H. L. Reed & E. B. White, "Stability and Transition of Three-Dimensional Boundary Layers," *Annual Review of Fluid Mechanics*, Vol. 35, 2003, pp. 413-440.

[15] E. Reshotko & A. Tumin, "Role of Transient Growth in Roughness-Induced Transition", *AIAA Journal*, Vol. 42, No. 4, April 2004, pp. 766-770.

[16] C. Chang & M. Choudhari, "Hypersonic Viscous Flow over Large Roughness Elements", AIAA 2009-0173

[17] P.M. Danehy, A.P. Garcia, S. Borg, A.A. Dyakonov, S.A. Berry, J.A. (Wilkes) Inman & D. W. Alderfer, "Flourescence visualization of hypersonic flow past triangular and rectangular boundary-layer trips," AIAA-2007-0536, 45th AIAA Aerospace Sciences Meeting, Reno Nevada, January 8-11(2007).

[18] M. D. Bartkowicz, P. K. Subbareddy & G. V. Candler, "Numerical Simulations of Roughness Induced Instability in the Purdue Mach 6 Wind Tunnel", AIAA-2010-4723.

[19] C. J. Baker, "The laminar horseshoe vortex", *Journal of fluid mechanics*, Vol. 95, part 2, pp. 347-367, 1979.

[20] B. M. Wheaton & S. P. Schneider, "Roughness-Induced Instability in a Laminar Boundary Layer at Mach 6", AIAA-2010-1574.

[21] J. A. Redford, N. D. Sandham & G. T. Roberts, "Roughness-induced transition of compressible laminar boundary layers", Proceedings of the Seventh IUTAM Symposium on Laminar-Turbulent Transition, Stockholm, Sweden, 2009.

[22] P. S. Iyer, S. Muppidi & K. Mahesh, "Transition of hypersonic flow past flat plate with roughness elements", AIAA-2010-5015.

[23] O. Marxen & G. Iaccarino, "Numerical Simulation of the effect of a roughness element on high-speed boundary layer instability", AIAA-2008-4400.

[24] G. Groskopf, M. J. Kloker & O. Marxen, "Bi-global secondary stability theory for high-speed boundary-layer flows", *Center for Turbulence Research Proceedings of the Summer Program 2008.*

[25] N. Park & K. Mahesh, "Numerical and modeling issues in LES of compressible turbulent flows on unstructured grids", *AIAA* paper-722, 2007.

[26] P. M. Danehy, Personal communication.

[27] M. S. Loginov, N. A. Adams & A. A. Zheltovodov, 2006 Large–eddy simulation of shock-wave/turbulent-boundary-layer interaction *J. Fluid. Mech* **565:**135–169.

[28] A. A. Zheltovodov, V. M. Trofimov, E. Schulein & V. N. Yakovlev, 1990 An experimental documentation of supersonic turbulent flows in the vicinity of forward- and backward-facing ramps. *Tech. Rep.* 2030. Institute of Theoretical and Applied Mechanics, USSR Academy of Sciences, Novosibirsk.

[29] P. B. Bookey, C. Wyckham, A. J. Smits & M. P. Martin, 2005 New Experimental data of STBLI at DNS/LES accessible Reynolds numbers *AIAA Paper* 2005–309.

[30] M. J. Ringuette, P. B. Bookey, W. Wyckham & A. J. Smits, 2009 Experimental study of a Mach 3 compression ramp interaction at $Re_\theta = 2400$. *AIAA J.* **47:**373–385.